THE JOURNAL OF PHYSICAL CHEMISTRY Letters

pubs.acs.org/JPCL

Letter

Controlling the Energy-Level Alignment of Silicon Carbide Nanocrystals by Combining Surface Chemistry with Quantum Confinement

Atta Ul Haq, Marius Buerkle, Sadegh Askari, Conor Rocks, Chengsheng Ni, Vladimir Švrček, Paul Maguire, John T. S. Irvine, and Davide Mariotti*

Cite This: *J. Phys. Chem. Lett.* 2020, 11, 1721−1728

Read Online

ACCESS | Metrics & More | Article Recommendations | Supporting Information

ABSTRACT: The knowledge of band edges in nanocrystals (NCs) and quantum-confined systems is important for band alignment in technologically significant applications such as water purification, decomposition of organic compounds, water splitting, and solar cells. While the band energy diagram of bulk silicon carbides (SiCs) has been studied extensively for decades, very little is known about its evolution in SiC NCs. Moreover, the interplay between quantum confinement and surface chemistry gives rise to unusual electronic properties and remains barely understood. Here, we report for the first time the complete band energy diagram of SiC NCs synthesized such that they span the regime from strong to intermediate to weak quantum confinement. The absolute positions of the highest occupied (HOMO) and lowest unoccupied (LUMO) molecular orbitals show clear size dependence. While the HOMO level follows the expected behavior for quantum-confined electronic states, the LUMO energy shifts below the bulk conduction band minimum, which cannot be explained by a simple quantum confinement caused by the size effect. We show that this effect is a result of the interplay between quantum confinement and the formation of surface states due to partial and site-selective oxygen passivation.

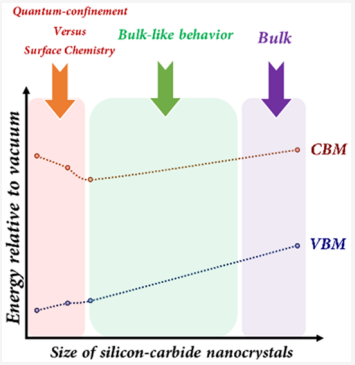

Over the past few decades, bandgap engineering, the ability to tailor the bandgap of nanoscale semiconductors, has inspired considerable excitement because of the visionary technological opportunities it presents.[1−3] The relatively easy access to bandgap measurement techniques has contributed to the understanding of bandgap widening, due to quantum confinement, and the exploitation of this phenomenon. However, the full energy band diagram (EBD) requires accurate knowledge of a range of other critical parameters in addition to the bandgap. These include the conduction and valence band-edge locations [or highest occupied molecular and lowest unoccupied molecular orbital (HOMO and LUMO, respectively) as appropriate[a]] and Fermi level; together, these are decisive for a very wide range of applications. The impact of quantum confinement on these energy band parameters has received little attention, in part due to measurement challenges as well as the higher sensitivity and precision required. Nonetheless, tailoring the corresponding EBD energy levels through quantum confinement is in effect a new and much more powerful tool that offers the opportunity for EBD and band alignment engineering to complement the traditional bandgap engineering.

The changes in the absolute position of the band edges and Fermi level of quantum-confined systems are key to the governing criteria in designing appropriate materials for most applications with technological significance. Band alignment,[4−6] charge injection,[7] and controlling charge recombination[8] have been demonstrated in nanocrystals for solar cell applications and highlight the importance of the band-edge alignment and/or location for device performance. Water splitting upon light absorption,[9,10] reduction of CO_2,[11] and purification of polluted water[12] are further examples where the positions of the band edges have been shown to be important.

Given the technological significance of band-edge positions of SiC in various industrial applications, we report here, for the first time, the complete EBD and size-dependent shifts in the absolute energy levels of SiC NCs that are affected by quantum confinement. We debate the use of various experimental techniques for the measurement of the corresponding critical parameters. We carry out theoretical calculations that reveal the influential role of surface states, which could be harnessed as a powerful design parameter. While our work is applied here to SiC NCs, the quest for detailed information about the EBD is relevant for most quantum-confined and nanoscale systems and has a dramatic impact on a very wide range of energy applications.

SiC Nanocrystal (NC) Synthesis. Silicon carbide (SiC) is an important member of the group IV semiconducting materials

Received: December 23, 2019
Accepted: February 10, 2020
Published: February 10, 2020

https://dx.doi.org/10.1021/acs.jpclett.9b03828
J. Phys. Chem. Lett. 2020, 11, 1721−1728

with a wide variety of applications of technological importance. SiC has excellent electronic, chemical, thermal, and mechanical stabilities that are best suited for next-generation high-power, high-temperature, and high-frequency applications and other industrial scale applications.[13−16] SiC can crystallize into various structures showing polytypism. Polytypism in SiC is due to a range of possible stacking sequences of Si−C layers, and among hundreds of polytypes, 3C-SiC, 4H-SiC, and 6H-SiC are the notable ones.[14] SiC NCs can be synthesized from a tetramethylsilane (TMS) precursor utilizing an atmospheric-pressure microplasma process. Our research on the synthesis of SiC NCs with this method has demonstrated a high degree of reliability in producing high-quality NCs supported by full and in-depth characterization of materials[17] (see also Figure S1). Cubic (3C-SiC) SiC NCs with different mean diameters of 1.5, 3.7, and 5.3 nm and with narrow size distributions were previously achieved under different synthesis conditions. We therefore relied on this method to produce size-tunable cubic SiC (3C-SiC) NCs and to study their electronic properties. Our further analysis has demonstrated the repeatability of our process and therefore confirmed the morphological, chemical, and structural composition of the SiC NCs. Representative high-resolution transmission electron microscopy (HR-TEM) images of SiC NCs are shown in panels a, d, and g of Figure 1. The corresponding FFT images are displayed in the inset images of panels a, d, and g of Figure 1. The inverse FFT images are constructed by applying masking (inset images) to the corresponding FFTs as shown in panels b, e, and h of Figure 1, respectively. The line profiles of the inverse FFTs of SiC NCs are shown in panels c, f, and i of Figure 1, which confirm the lattice spacing of the (200) planes. Despite being very small, NCs are crystalline as represented by their lattice fringes of cubic SiC (3C-SiC). X-ray photoelectron spectroscopy and Fourier transform infrared spectroscopy (FTIR) have revealed H-terminations to be present at the surface for the most part, with both C−H_x and Si−H_x bonds.[17] Further FTIR (Figure S2) has confirmed the formation of Si−C bonds as the respective peaks at around 780 cm^{-1} could be easily observed. Widespread Si−H/C−H passivation is also confirmed, and no peaks indicating bonding between C and O could be detected. Stoichiometric silicon oxide generally presenta a peak at 1070 cm^{-1}, which broadens asymmetrically when bonds are strained and/or nonstoichiometric oxide is present.[18,19] On this basis, the relatively sharp peak at ∼1020 cm^{-1} is not consistent with Si−O−Si bonding arrangements and it is therefore assigned to the contribution of both C−H_2 and Si═O. While the presence of Si−O−Si networks was excluded by extensive oxidation, the analysis concluded that minor and selective oxidation of surface Si atoms with a carbon back bond (i.e., C−Si−O) was present.

The mechanisms leading to the formation of SiC NCs from TMS in the atmospheric-pressure microplasma (Figure 2) differ from the standard nucleation and growth steps required in equilibrium thermodynamic processes. The plasma environment initially leads to the fragmentation of TMS with the loss of methyl groups.[20−22] As the fragmentation is for the most part due to electron-induced dissociation, the formation and growth of the NCs progress through a gas-phase polymerization chain process, confirmed by the close stoichiometry of the NCs. This is similar to that observed for silane low-pressure plasmas;[23,24] however, at atmospheric pressure, ions are expected to play a minor role while neutrals are mainly the ones that participate in the gas-phase polymerization process.

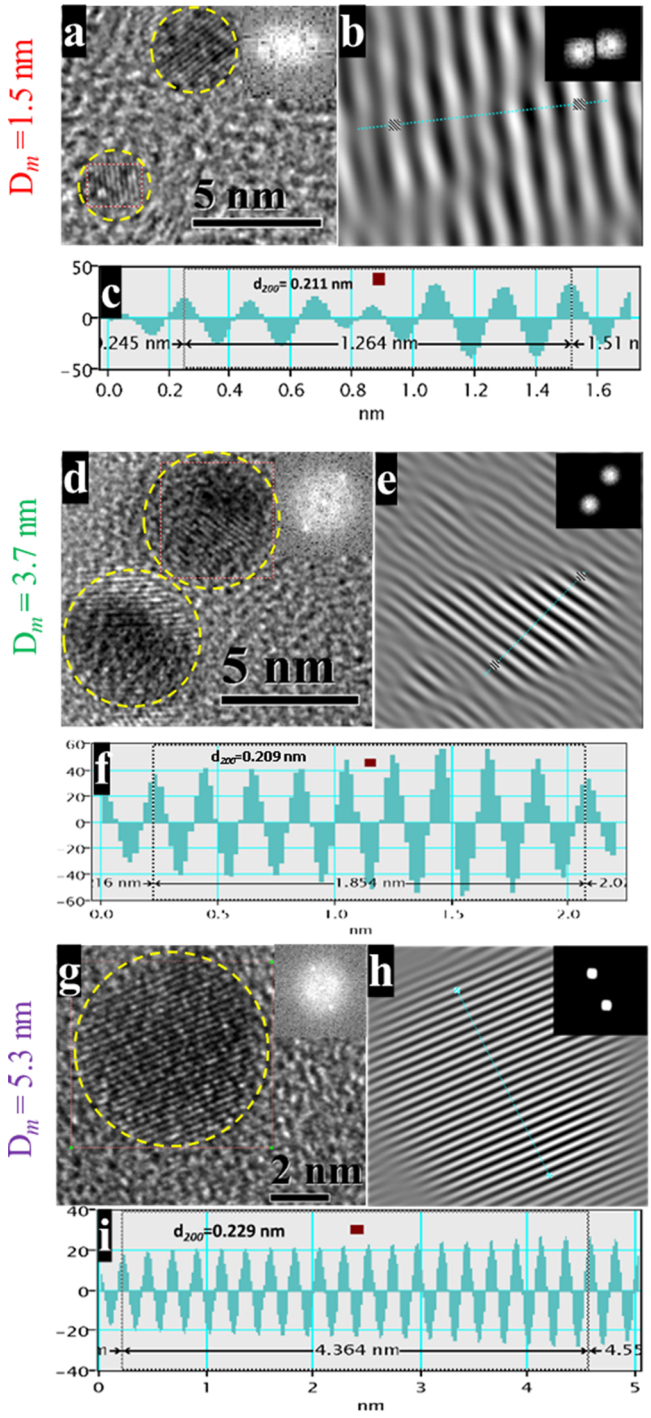

Figure 1. (a−c) High-resolution transmission electron microscopy (HR-TEM) micrograph of 1.5 nm (mean diameter, D_m) SiC nanocrystals with the fast Fourier transform (FFT) image (inset), inverse FFT obtained by masking the FFT (inset), and the corresponding line profile, respectively. (d−f) HR-TEM micrograph of 3.7 nm (D_m) SiC NCs with the FFT image (inset), inverse FFT with the masked pattern (inset), and the corresponding line profile, respectively. (g−i) HR-TEM micrograph of 5.3 nm (D_m) SiC NCs with the FFT image (inset), inverse FFT with the masked pattern (inset), and the corresponding line profile, respectively.

The fragments contributing to the growth are mainly $Si(CH_3)_{4-x}$ and $HSi(CH_3)_{4-x}$, where x represents the number of methyl groups lost by the TMS molecules. The polymerization and formation of the Si−C structure are the result of

https://dx.doi.org/10.1021/acs.jpclett.9b03828
J. Phys. Chem. Lett. 2020, 11, 1721−1728

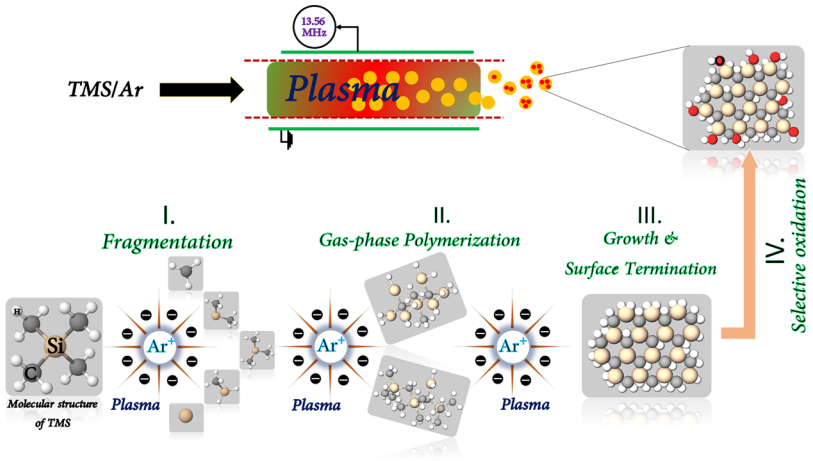

Figure 2. Schematic diagram illustrating the fragmentation of tetramethylsilane (TMS) leading to the nucleation and growth of silicon carbide nanocrystals in the atmospheric-pressure plasma process.

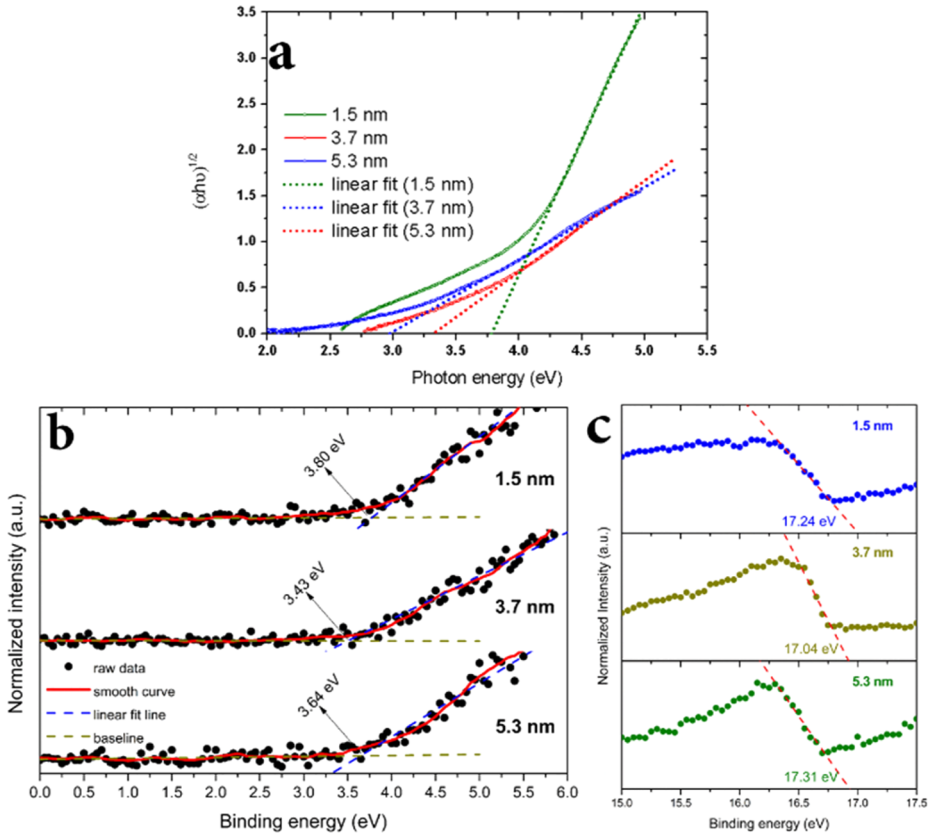

Figure 3. (a) HOMO−LUMO gaps of SiC nanocrystals (NCs) determined from the Tauc plots. (b) Ultraviolet photoelectron spectroscopy (UPS) spectra of the onset region of SiC NCs. The onset has been evaluated by applying a linear fit to the data and determining the intercept; here the baseline has been corrected after smoothing (Savitzky−Golay smoothing method) the data points for a more accurate background removal. (c) UPS spectra of the secondary electron-edge region of SiC NCs. The cutoff has been determined by applying a linear fitting to the negative slope that allowed us to determine the intercept to the axis as shown.

the reaction of the Si− or Si−H terminations on the methyl or CH_y groups of the polymerized products; in particular, reactions with $HSi(CH_3)_{4-x}$ also result in the formation of molecular H_2. This leads to a growing Si−C network with H-terminations on the carbon atoms. The silicon atoms at the surface however easily lose the methyl groups and therefore can form dangling surface bonds prone to oxidation when exposed to the environment. The required energy for crystallization is then supplied by selective particle heating within the plasma.[25] This is due to ion bombardment and recombination at the surface of the particles, which can lead to a nanoparticle temperature hundreds of kelvin higher than the surrounding gas-phase temperature.[23]

Electronic Properties (experimental). To evaluate the size-dependent energy band diagram, we have experimentally measured the absolute position of the Fermi level and the positions of the HOMO and the LUMO levels, as these vary for NCs of different sizes. It is however instructive to compare

https://dx.doi.org/10.1021/acs.jpclett.9b03828
J. Phys. Chem. Lett. 2020, 11, 1721−1728

the size of the NCs to the Bohr exciton radius (a_0 = 2.0 nm) for 3C-SiC. The mean radius $r_{d=1.5\ nm}$ of 0.75 nm of the smallest SiC NCs (Figure 1a–c) is much smaller than a_0; thus, we expect these smaller NCs to be within the strong quantum confinement regime. For the SiC NCs with an $r_{d=3.7\ nm}$ of 1.85 nm (Figure 1d–f), the radius is comparable to the exciton radius and we can expect quantum confinement to be weaker but effective. The radius $r_{d=5.3\ nm}$ of 2.65 nm of the largest SiC NCs (Figure 1g–i) is larger than a_0, and we can expect that the effect of the quantum confinement is further reduced; however, while we tend toward bulk properties, finite size effects remain present.

The different polytypes of bulk SiC can exhibit drastically different properties; e.g., the bandgap can vary between 2.2 and 3.3 eV.[14,26] The valence band maximum (VBM) positions of SiC, in their bulk form, have been reported to be around 6–6.5 eV,[27−32] and the VBM lies in the same location (T point) of the Brillouin zone for most of the polytypes.[33] On the other hand, the locations of the conduction band minima (CBM) are not the same for all polytypes,[33,34] due to the variation in their crystal structures.[35] In a majority of the cases, however, band diagrams determined from either theoretical or experimental efforts are based on the bulk values of the respective polytypes.[33,34,36−41] To date, there have been no reports on the experimental determination of SiC NC band-edge positions under quantum confinement. These positions can be acquired in bulk materials using X-ray absorption spectroscopy (XAS),[42] ultraviolet photoelectron spectroscopy (UPS),[6,43,44] photoemission spectroscopy in air (PESA),[45] cyclic voltammetry (CV),[46] and potential-dependent absorption spectroscopy.[47] Most commonly, UPS measurements have been reported for accurate determination of HOMO levels (VBM).[48]

Here, the electronic gap and levels of these SiC NCs were evaluated by measuring the optical transmission characteristics of the SiC NCs. Depending on the particle diameter, the transmission spectra of the SiC NCs show a clear blue-shift in the transmission with a decrease in the size of the SiC NCs (Figure S3). The corresponding HOMO–LUMO gaps determined from the Tauc plots are shown in Figure 3a and are summarized in Table 1.

Table 1. Size Dependence of the HOMO–LUMO Gap (bandgap), Fermi Energy (E_F), HOMO Energy (VBM), and LUMO Energy (CBM) Along with the Corresponding Values of Bulk 3C-SiC[a]

NC mean diameter (nm)	bandgap (eV)	E_F (eV)	HOMO (VBM) (eV)	LUMO (CBM) (eV)
1.5	3.78	−4.86	−7.76	−3.98
3.7	3.32	−5.39	−7.59	−4.27
5.3	2.97	−5.45	−7.53	−4.56
bulk	2.35	−4.60	−6.18	−3.83

[a]Bulk values are also reported.[50−52].

Our SiC NCs not only exhibited quantum confinement on the HOMO–LUMO gap but also demonstrated a strong dependence of the Fermi level and of the absolute HOMO and LUMO positions. The corresponding Fermi levels (E_F) are obtained by Kelvin probe measurements (Figure S4) and are summarized in Table 1. A shift of the Fermi level is expected due to the change in the sizes of the NCs and may also be due to a contribution from the surface functionalities.[49]

The absolute position of the HOMO is obtained from UPS by determining the onset of the binding energy (E_{onset}) and the secondary electron energy cutoff ($E_{SE\text{-}cutoff}$), also explained in the Supporting Information. Figure 3b shows the E_{onset} values extracted from the UPS spectra, and Figure 3c represents the $E_{SE\text{-}cutoff}$ values of the SiC NCs. The HOMO energy is

$$E_{HOMO} = h\nu - (E_{SE\text{-}cutoff} - E_{onset}) \quad (1)$$

where $h\nu$ is the energy of helium I (21.2 eV). HOMO energies extracted from UPS are summarized in Table 1. Finally, the LUMO energy (Table 1) is calculated by adding the bandgap value to the HOMO level. Table 1 therefore provides the full experimental details of the EBD for the SiC NCs of different sizes.

Figure 4 depicts the corresponding EBDs ("Experiment", red) as per values in Table 1 and compares them with the bulk EBD values (in black on the left of Figure 4); the values from theoretical calculations ("Theory-GW", blue) for 1.5 nm diameter SiC NCs are discussed below. We first note that, as expected, decreasing the diameter of the NCs, i.e., increasing the quantum confinement, opens the bandgap. The largest NCs present the smallest bandgap (2.97 eV) of all of the NCs; this is close to but still larger than the bulk bandgap value (2.35 eV). The positioning of the HOMO and LUMO levels for all NCs follows the expected quantum confinement behavior as previously outlined in relation to the relationship between the particle diameter and the Bohr radius, i.e., HOMO moving up in energy toward the bulk VBM and LUMO energy decreasing with the particle diameter increasing. However, when NC energy levels are compared to the bulk values, these appear to be all downshifted on the energy scale so that the HOMO level of the largest NCs is still >1 eV away from the bulk limit and all of the LUMO energies are lower than the bulk CBM. This behavior suggests that, in addition to quantum confinement, other factors contribute to the position of the EBD levels for the NCs.

Electronic Structure Calculations Based on First Principles. To clarify the experimental results, we performed first-principles electronic structure calculations at the PBE+G0W0 level. We consider here only the smallest particle diameter as an example and take into account partial oxygen surface coverage following our FTIR measurements, where oxygen is preferentially bound to Si and not to C as suggested by our experimental characterization of materials. The shape of the FTIR signal just above 1000 cm^{-1}, the presence of Si–H_x and C–H_y terminations, and the surface structure of SiC NCs suggest that Si=O bonds are more likely than an extended Si–O–Si surface network (see the Supporting Information). Furthermore, Si–O–Si does not largely influence the excitation spectrum of SiC NCs.[53] We therefore focus here on SiC NCs with hydrogen atoms on all surface carbon atoms and on all highly coordinated silicon surface atoms (i.e., silicon atoms with a single dangling bond), while oxygen is on under-coordinated surface silicon atoms (i.e., Si=O bonds). This corresponds to an oxygen coverage of 10% with respect to H-terminations. The NCs are modeled such that we start with the Si and C atoms at ideal 3C-SiC lattice positions and surface atoms terminated as described above. The structures are subsequently relaxed (see Methods). While we observe a certain surface relaxation, the lattice stays close to the bulk values, which is fully consistent with our HR-TEM measurements and experimental[17,54] and first-principles[54,55] data in the literature.

https://dx.doi.org/10.1021/acs.jpclett.9b03828
J. Phys. Chem. Lett. 2020, 11, 1721−1728

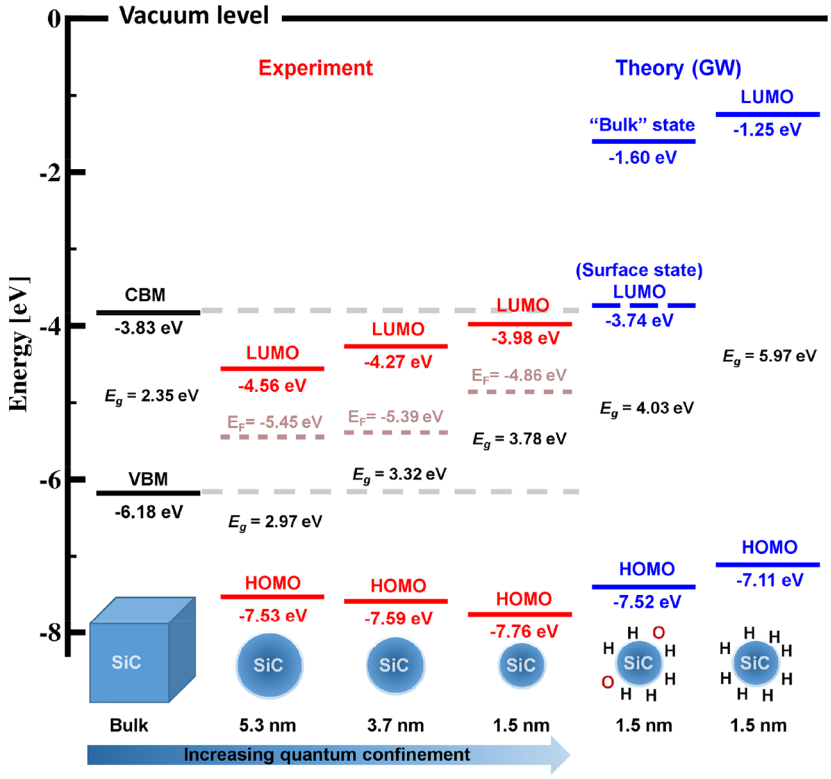

Figure 4. Energy band diagrams showing the VBM/HOMO, CBM/LUMO, Fermi energy (E_F), and bandgap (E_g) for bulk SiC (black, left side), for experimental SiC NCs with mean diameters of 1.5, 3.7, and 5.3 nm ("Experiment", red), and from calculations of 1.5 nm SiC NCs with hydrogen terminations and with partial Si=O surface coverage ("Theory-GW", blue).

The results of our calculation for H-terminated SiC NCs are shown in Figure 4 ("Theory-GW", blue; EBD on the right). We can initially compare the calculated HOMO−LUMO gap of these H-terminated NCs with a simple estimate of NC bandgap E_{NC}^{gap} based on the Brus equation[56] $E_{NC}^{gap}(r) \approx E_{bulk}^{gap} + \frac{h^2}{8r^2}\left(\frac{1}{m_e^*} + \frac{1}{m_h^*}\right) - \frac{1.8e^2}{4\pi\varepsilon_r\varepsilon_0 r}$ where h is Planck's constant, e the electron charge, ε_0 the vacuum permittivity, and r the particle radius. Using literature values for the bulk bandgap (2.35 eV), effective electron mass m_e^* ($0.347m_0$) and effective hole mass m_h^* ($0.45m_0$), and dielectric constant of bulk SiC (ε_r = 9.52),[57] we find that the bandgap for a NC with a radius r of 0.75 nm (d = 1.5 nm) is E_{NC}^{gap} (0.75 nm) = 5.7 eV; this compares well to our GW result of 5.97 eV. Our calculations for H-terminated NCs are also consistent with the effects of strong quantum confinement, where the LUMO is upshifted in the energy scale compared to the bulk value much more than the HOMO level is downshifted and with an overall increase in the bandgap, i.e., from 2.35 to 5.97 eV. However, the measured bandgap value of 3.78 eV for the 1.5 nm diameter SiC NCs (Figure 4, red) is much smaller than the results of our calculations (5.97 eV). Moreover, we stress again that the measured HOMO/LUMO levels of the NCs appear to be all lower in energy than what would be expected if only quantum confinement was to be considered and with the LUMO level by far lower (−3.98 eV) than the calculated value (−1.25 eV).

We therefore have to conclude that the H-terminated NC model does not represent well the experimental SiC NCs, and consequently, we have carried out calculations to take into consideration partial Si=O surface coverage as previously anticipated. We find that oxygen atoms in the Si=O sites induce surface states with energies inside the HOMO−LUMO gap (Figure 5) that drastically downshifts the LUMO level on

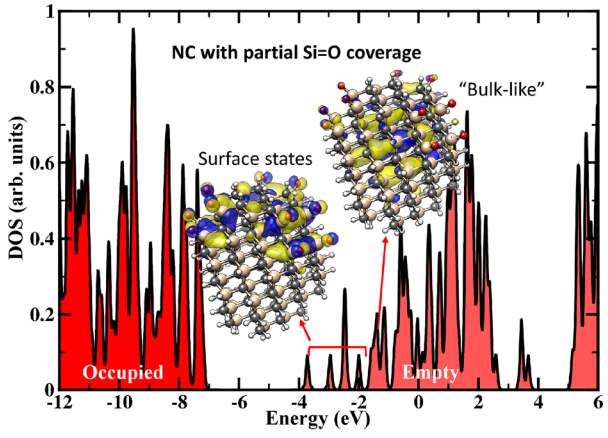

Figure 5. Calculated density of states of the SiC NC with oxygen coverage on double bond sites. The states inside the gap are related to O-induced surface states, and the edge at a higher energy is given by oxygen-independent "bulk"-like states.

the energy scale and effectively reduces the bandgap of the NCs. Moreover, also the HOMO level is slightly downshifted in energy due to charge transfer between the oxygen and the SiC NCs, an effect observed recently also for elemental Si NCs.[49] The overall results of these calculations show that SiC NCs with partial Si=O coverage are a much better match in terms of HOMO/LUMO levels and bandgap (see Figure 4). This, together with the chemical analysis of the SiC NCs,

https://dx.doi.org/10.1021/acs.jpclett.9b03828
J. Phys. Chem. Lett. 2020, 11, 1721−1728

suggests that the experimentally observed EBD energies are related to surface states induced by oxygen.

A full EBD of 3C-SiC NCs has been presented for the first time with the experimental measurements of absolute band-edge positions of different sizes of SiC NCs. Quantum confinement has been confirmed together with an overall increasing trend of the bandgap. The HOMO and LUMO energy positions have also presented consistent shifts that in part are attributed to the quantum confinement regimes, as well. However, to explain some of the trends observed in the experimental measurements, partial oxygen passivation was considered and supported by chemical analysis of the SiC NCs. This hypothesis was then further reinforced with theoretical calculations that clearly showed the impact of partial Si═O surface coverage. The HOMO of SiC NCs with partial oxidation has shifted >1.5 eV with respect to the absolute VBM position of bulk SiC (3C-SiC), thereby offering application opportunities. Furthermore, the Fermi levels have also shown a size-dependent behavior by shifting toward the LUMO levels when the size of SiC NCs is decreased. While our work was focused on SiC NCs, our results have much wider implications. First, the possibility of engineering band-edge absolute values opens great opportunities in EBD and band alignment engineering. Second, we have highlighted opportunities and challenges in measurement techniques that require more attention for their application to nanoparticle systems.

METHODS

Preparation of SiC NCs. The synthesis of SiC NCs was carried out in a plasma reactor operated at atmospheric pressure following our previous work.[17] The precursor for SiC was tetramethylsilane (TMS), which was purchased from Sigma-Aldrich. Argon gas was bubbled through the TMS at flow rates of 0.4, 2.4, and 5 sccm. The plasma reactor consists of a rectangular hollow glass with two flat electrodes (20 mm × 5 mm); one of the electrodes was grounded, while the other was used to sustain the plasma by applying the radiofrequency (RF) power (100 W) at 13.56 MHz. The SiC NCs were collected directly in colloids in ethanol or deposited directly on a substrate.

Material Characterization and Band Energy Diagram Measurements. Structural investigation of the SiC NCs was carried out using transmission electron microscopy (JEOL JEM-2100F instrument operated at 200 kV). The samples for TEM were prepared by drop-casting (~6 drops) SiC NC/ethanol colloids onto the TEM grids. The chemical structure and Si−C bonding were confirmed using Fourier transform infrared spectroscopy (FTIR) equipped with an attenuated total reflection (ATR) accessory (Thermofisher iD5). SiC NCs (in solid form) were directly placed on top of the diamond crystal of the ATR accessory, and then the measurements were taken. An ultraviolet/visible (UV/vis) spectrometer (PerkinElmer Lambda 35) was used for the transmission measurements of SiC NCs. The SiC NCs were collected directly in ethanol from the plasma for UV/vis measurements. The measurement of the Fermi level was taken using an SKP Kelvin probe system with gold as a reference electrode. The samples for the Kelvin probe were prepared by depositing SiC NCs directly from the plasma onto glass substrates coated with a conductive indium−tin oxide (ITO) layer. The HOMO energy levels of SiC NCs were estimated by UPS and X-ray photoelectron spectroscopy (XPS). UPS data of SiC NCs samples prepared on ITO-coated glass substrates were acquired using He−I (21.2 eV) beam excitation source. The XPS spectra were acquired using Kratos equipment (Axis Ultra DLD photoelectron spectrometer) with an X-ray source of Al Kα radiation (1486 eV). The spectra were collected at a resolution of 0.05 eV and a pass energy of 40 eV operating at 10^{-9} bar. The C 1s peak at 284.8 eV was taken for calibrating the spectra.

First-Principles Calculations. The electronic and geometrical properties of the SiC NCs were obtained within density functional theory at the PBE level of theory[58] using the def2-SV(P) basis set and the corresponding ri-basis set.[59,60] The total energy calculations were converged with a precision of 10^{-7} au. To model the nanocrystal geometry, we generate an initial structure with a certain diameter cut out from a cubic SiC (3C-SiC) lattice with low-coordinated surface atoms, removed such that only single and double dangling bonds remain. As described in Electronic Structure Calculations Based on First Principles, the surface atoms are passivated with either hydrogen or oxygen. The SiC NCs were fully relaxed, and the structural optimization was carried out until the maximum norm of the gradient dropped below 1×10^{-5} au. The resulting structure remains, consistent with experiment, close to the 3C-SiC lattice. The quasiparticle energies were obtained at the G0W0 level.[61−63] All calculations were carried out using the quantum chemistry package TURBOMOLE.[64] While the employed basis set cannot be expected to give completely converged GW quasiparticle energy with regard to the basis set limit, the expected errors[64] are much smaller than the energy differences discussed here and the discussion of underlying physical and chemical mechanisms remains valid.

ASSOCIATED CONTENT

Supporting Information

The Supporting Information is available free of charge at https://pubs.acs.org/doi/10.1021/acs.jpclett.9b03828.

TEM images, FTIR spectra, UV/vis spectra, Kelvin probe measurements, HOMO/LUMO measurements, full EBD construction procedure, summary table of EBD, and significance of EBD of SiC NCs (PDF)

AUTHOR INFORMATION

Corresponding Author

Davide Mariotti − *Nanotechnology & Integrated Bioengineering Centre (NIBEC), Ulster University, Newtownabbey BT37 0QB, United Kingdom;* orcid.org/0000-0003-1504-4383; Email: d.mariotti@ulster.ac.uk

Authors

Atta Ul Haq − *Nanotechnology & Integrated Bioengineering Centre (NIBEC), Ulster University, Newtownabbey BT37 0QB, United Kingdom;* orcid.org/0000-0002-3942-6290

Marius Buerkle − *National Institute of Advanced Industrial Science and Technology (AIST), Tsukuba 305-8568, Japan;* orcid.org/0000-0003-3464-2549

Sadegh Askari − *Institute for Experimental and Applied Physics, Christian-Albrechts-Universität zu Kiel, 24118 Kiel, Germany;* orcid.org/0000-0001-7267-7510

Conor Rocks − *Nanotechnology & Integrated Bioengineering Centre (NIBEC), Ulster University, Newtownabbey BT37 0QB, United Kingdom*

https://dx.doi.org/10.1021/acs.jpclett.9b03828
J. Phys. Chem. Lett. 2020, 11, 1721−1728

Chengsheng Ni − *School of Chemistry, University of St Andrews, St Andrews, Fife KY16 9ST, United Kingdom; College of Resources and Environment, Southwest University, 400715 Chongqing, China;* orcid.org/0000-0002-7184-1654
Vladimir Švrček − *National Institute of Advanced Industrial Science and Technology (AIST), Tsukuba 305-8568, Japan*
Paul Maguire − *Nanotechnology & Integrated Bioengineering Centre (NIBEC), Ulster University, Newtownabbey BT37 0QB, United Kingdom;* orcid.org/0000-0002-2725-4647
John T. S. Irvine − *School of Chemistry, University of St Andrews, St Andrews, Fife KY16 9ST, United Kingdom;* orcid.org/0000-0002-8394-3359

Complete contact information is available at: https://pubs.acs.org/10.1021/acs.jpclett.9b03828

Notes

The authors declare no competing financial interest.

■ ACKNOWLEDGMENTS

This work was supported by the Marie Curie Initial Training Network (RAPID-ITN, Grant 606889) and by EPSRC (Grants EP/K022237/1 and EP/M024938/1). A.U.H. and S.A. are thankful for the financial support from RAPID-ITN and Ulster University's Vice Chancellor scholarships, respectively.

■ ADDITIONAL NOTE

[a]Quantum confinement produces important changes in the density of states. These contribute to a transition from the bulk description of the band energy diagram (i.e., conduction band, valence band, and Fermi level) to a molecular description of discrete energy levels, i.e., with the definition of the highest occupied molecular orbital (HOMO) and the lowest unoccupied molecular orbital (LUMO).

■ REFERENCES

(1) Bera, D.; Qian, L.; Tseng, T. K.; Holloway, P. H. Quantum Dots and Their Multimodal Applications: A Review. *Materials* **2010**, *3*, 2260−2345.
(2) Capasso, F. Band-Gap Engineering: From Physics and Materials to New Semiconductor Devices. *Science* **1987**, *235* (4785), 172−176.
(3) Smith, A. M.; Nie, S. Semiconductor Nanocrystals: Structure, Properties, and Band Gap Engineering. *Acc. Chem. Res.* **2010**, *43* (2), 190−200.
(4) Kamat, P. V. Quantum Dot Solar Cells. Semiconductor Nanocrystals as Light Harvesters †. *J. Phys. Chem. C* **2008**, *112* (48), 18737−18753.
(5) Kameyama, T.; Douke, Y.; Shibakawa, H.; Kawaraya, M.; Segawa, H.; Kuwabata, S.; Torimoto, T. Widely Controllable Electronic Energy Structure of ZnSe−AgInSe 2 Solid Solution Nanocrystals for Quantum-Dot-Sensitized Solar Cells. *J. Phys. Chem. C* **2014**, *118* (51), 29517−29524.
(6) Chuang, C.-H. M.; Brown, P. R.; Bulović, V.; Bawendi, M. G. Improved Performance and Stability in Quantum Dot Solar Cells through Band Alignment Engineering. *Nat. Mater.* **2014**, *13*, 796.
(7) Salant, A.; Shalom, M.; Tachan, Z.; Buhbut, S.; Zaban, A.; Banin, U. Quantum Rod-Sensitized Solar Cell: Nanocrystal Shape Effect on the Photovoltaic Properties. *Nano Lett.* **2012**, *12* (4), 2095−2100.
(8) Zhao, K.; Pan, Z.; Zhong, X. Charge Recombination Control for High Efficiency Quantum Dot Sensitized Solar Cells. *J. Phys. Chem. Lett.* **2016**, *7* (3), 406−417.
(9) Pan, H. Principles on Design and Fabrication of Nanomaterials as Photocatalysts for Water-Splitting. *Renewable Sustainable Energy Rev.* **2016**, *57*, 584−601.
(10) Zhang, Y.; Xia, T.; Wallenmeyer, P.; Harris, C. X.; Peterson, A. A.; Corsiglia, G. A.; Murowchick, J.; Chen, X. Photocatalytic Hydrogen Generation from Pure Water Using Silicon Carbide Nanoparticles. *Energy Technol.* **2014**, *2* (2), 183−187.
(11) Li, H.; Lei, Y.; Huang, Y.; Fang, Y.; Xu, Y.; Zhu, L.; Li, X. Photocatalytic Reduction of Carbon Dioxide to Methanol by Cu2O/SiC Nanocrystallite under Visible Light Irradiation. *J. Nat. Gas Chem.* **2011**, *20* (2), 145−150.
(12) Yamashita, H.; Nishida, Y.; Yuan, S.; Mori, K.; Narisawa, M.; Matsumura, Y.; Ohmichi, T.; Katayama, I. Design of TiO2-SiC Photocatalyst Using TiC-SiC Nano-Particles for Degradation of 2-Propanol Diluted in Water. *Catal. Today* **2007**, *120* (2), 163−167.
(13) Bhatnagar, M.; Baliga, B. J. Comparison of 6H-SiC, 3C-SiC, and Si for Power Devices. *IEEE Trans. Electron Devices* **1993**, *40* (3), 645−655.
(14) Morkoç, H.; Strite, S.; Gao, G. B.; Lin, M. E.; Sverdlov, B.; Burns, M. Large-Band-Gap SiC, III-V Nitride, and II-VI ZnSe-Based Semiconductor Device Technologies. *J. Appl. Phys.* **1994**, *76* (3), 1363−1398.
(15) Harris, C. I.; Savage, S.; Konstantinov, A.; Bakowski, M.; Ericsson, P. Progress towards SiC Products. *Appl. Surf. Sci.* **2001**, *184* (1−4), 393−398.
(16) Ben-Zion, Y. Dynamic Rupture on an Interface between a Compliant Fault Zone Layer and a Stiffer Surrounding Solid. *J. Geophys. Res.* **2002**, *107* (B2), 2042.
(17) Askari, S.; Ul Haq, A.; Macias-Montero, M.; Levchenko, I.; Yu, F.; Zhou, W.; Ostrikov, K.; Maguire, P.; Svrcek, V.; Mariotti, D. Ultra-Small Photoluminescent Silicon-Carbide Nanocrystals by Atmospheric-Pressure Plasmas. *Nanoscale* **2016**, *8* (39), 17141−17149.
(18) Chou, J.; Lee, S. Effect of Porosity on Infrared-absorption Spectra of Silicon Dioxide. *J. Appl. Phys.* **1995**, *77* (4), 1805−1807.
(19) Pai, P. G.; Chao, S. S.; Takagi, Y.; Lucovsky, G. Infrared Spectroscopic Study of SiO x Films Produced by Plasma Enhanced Chemical Vapor Deposition. *J. Vac. Sci. Technol., A* **1986**, *4* (3), 689−694.
(20) Jauberteau, J. L.; Aubreton, J.; Jauberteau, I. Characterization of an Ar-TMS Microwave Discharge Using Mass Spectrometry: Effect of the Reactor Design on Free-Radical Contents. *Int. J. Mass Spectrom.* **1999**, *189* (1), 63−77.
(21) Basner, R.; Foest, R.; Schmidt, M.; Sigeneger, F.; Kurunczi, P.; Becker, K.; Deutsch, H. Electron Impact Ionization of Tetramethylsilane (TMS). *Int. J. Mass Spectrom. Ion Processes* **1996**, *153* (1), 65−78.
(22) McGinnis, S.; Riehl, K.; Haaland, P. D. Ion Chemistry in Tetramethylsilane (CH3)4Si. *Chem. Phys. Lett.* **1995**, *232* (1−2), 99−102.
(23) Kortshagen, U. R.; Sankaran, R. M.; Pereira, R. N.; Girshick, S. L.; Wu, J. J.; Aydil, E. S. Nonthermal Plasma Synthesis of Nanocrystals: Fundamental Principles, Materials, and Applications. *Chem. Rev.* **2016**, *116* (18), 11061−11127.
(24) Kortshagen, U. Nonthermal Plasma Synthesis of Semiconductor Nanocrystals. *J. Phys. D: Appl. Phys.* **2009**, *42* (11), 113001.
(25) Bapat, A.; Gatti, M.; Ding, Y.-P.; Campbell, S. A; Kortshagen, U. A plasma process for the synthesis of cubic-shaped silicon nanocrystals for nanoelectronic devices. *J. Phys. D: Appl. Phys.* **2007**, *40*, 2247−2257.
(26) Paufler, P. Landolt-Börnstein. Numerical Data and Functional Relationships in Science and Technology. New Series. Group III: Crystal and Solid State Physics. Vol. 22: Semiconductors. Subvolume a: Intrinsic Properties of Group IV Elements and III-V, II-VI and I-VII Co. *Cryst. Res. Technol.* **1988**, *23* (10−11), 1360−1360.
(27) Kumar, S.; Singh, J.; Akhtar, J. Materials and Processing for Gate Dielectrics on Silicon Carbide (SiC) Surface. In *Physics and Technology of Silicon Carbide Devices*; Hijikata, Y., Ed.; InTech, 2012. DOI: 10.5772/52553.
(28) Lüning, J.; Eisebitt, S.; Rubensson, J.-E.; Ellmers, C.; Eberhardt, W. Electronic Structure of Silicon Carbide Polytypes Studied by Soft X-Ray Spectroscopy. *Phys. Rev. B: Condens. Matter Mater. Phys.* **1999**, *59* (16), 10573−10582.

(29) Zhang, Y.; Lin, N.; Li, Y.; Wang, X.; Wang, H.; Kang, J.; Wilks, R.; Bär, M.; Mu, R. The Isotype ZnO/SiC Heterojunction Prepared by Molecular Beam Epitaxy - A Chemical Inert Interface with Significant Band Discontinuities. *Sci. Rep.* **2016**, *6* (March), 23106.
(30) Walsh, A.; Buckeridge, J.; Catlow, C. R. A.; Jackson, A. J.; Keal, T. W.; Miskufova, M.; Sherwood, P.; Shevlin, S. A.; Watkins, M. B.; Woodley, S. M.; et al. Limits to Doping of Wide Band Gap Semiconductors. *Chem. Mater.* **2013**, *25* (15), 2924−2926.
(31) Ashrafi, A. Band Offsets at ZnO/SiC Heterojunction: Heterointerface in Band Alignment. *Surf. Sci.* **2010**, *604* (21−22), L63−L66.
(32) Fan, H. B.; Sun, G. S.; Yang, S. Y.; Zhang, P. F.; Zhang, R. Q.; Wei, H. Y.; Jiao, C. M.; Liu, X. L.; Chen, Y. H.; Zhu, Q. S.; Wang, Z. G. Valence Band Offset of ZnO4H-SiC Heterojunction Measured by x-Ray Photoelectron Spectroscopy. *Appl. Phys. Lett.* **2008**, *92* (19), 192107.
(33) Choyke, W. J.; Devaty, R. P.; Sridhara, S. G. A Survey of Conduction and Valence Band Edges In. *Phys. Scr.* **1999**, *T79* (1), 9.
(34) Tallarida, M.; Schmeisser, D.; Zheng, F.; Himpsel, F. J. X-Ray Absorption and Photoemission Spectroscopy of 3C- and 4H-SiC. *Surf. Sci.* **2006**, *600* (18), 3879−3883.
(35) Park, C. H.; Cheong, B.-H.; Lee, K.-H.; Chang, K. J. Structural and Electronic Properties of Cubic, 2 H, 4 H, and 6 H SiC. *Phys. Rev. B: Condens. Matter Mater. Phys.* **1994**, *49* (7), 4485−4493.
(36) Persson, C.; Lindefelt, U.; Sernelius, B. E. Plasma-Induced Band Edge Shifts in 3C-, 2H-, 4H-, 6H−SiC and Si. *Solid-State Electron.* **2000**, *44* (3), 471−476.
(37) Persson, C.; Lindefelt, U.; Sernelius, B. E. Band Gap Narrowing in N-Type and p-Type 3C-, 2H-, 4H-, 6H-SiC, and Si. *J. Appl. Phys.* **1999**, *86* (8), 4419.
(38) Miedema, P. S.; Beye, M.; Könnecke, R.; Schiwietz, G.; Föhlisch, A. Thermal Evolution of the Band Edges of 6H-SiC: X-Ray Methods Compared to the Optical Band Gap. *J. Electron Spectrosc. Relat. Phenom.* **2014**, *197*, 37−42.
(39) Kityk, I.; Kassiba, A.; Plucinski, K.; Berdowski, J. Band Structure of Large-Sized SiC Nanocomposites. *Phys. Lett. A* **2000**, *265* (5−6), 403−410.
(40) Matos, M. Electronic Band Structure of 3C−SiC from Extended Hückel Theory. *J. Mol. Struct.: THEOCHEM* **1999**, *464* (1−3), 129−135.
(41) Ching, W. Y.; Xu, Y.-N.; Rulis, P.; Ouyang, L. The Electronic Structure and Spectroscopic Properties of 3C, 2H, 4H, 6H, 15R and 21R Polymorphs of SiC. *Mater. Sci. Eng., A* **2006**, *422* (1−2), 147−156.
(42) Lee, J. R. I.; Meulenberg, R. W.; Hanif, K. M.; Mattoussi, H.; Klepeis, J. E.; Terminello, L. J.; van Buuren, T. Experimental Observation of Quantum Confinement in the Conduction Band of CdSe Quantum Dots. *Phys. Rev. Lett.* **2007**, *98* (14), 146803.
(43) van Buuren, T.; Dinh, L. N.; Chase, L. L.; Siekhaus, W. J.; Terminello, L. J. Changes in the Electronic Properties of Si Nanocrystals as a Function of Particle Size. *Phys. Rev. Lett.* **1998**, *80* (17), 3803−3806.
(44) Macias-Montero, M.; Askari, S.; Mitra, S.; Rocks, C.; Ni, C.; Svrcek, V.; Connor, P. A.; Maguire, P.; Irvine, J. T. S.; Mariotti, D. Energy Band Diagram of Device-Grade Silicon Nanocrystals. *Nanoscale* **2016**, *8*, 6623−6628.
(45) Jasieniak, J.; Califano, M.; Watkins, S. E. Size-Dependent Valence and Conduction Band-Edge Energies of Semiconductor Nanocrystals. *ACS Nano* **2011**, *5* (7), 5888−5902.
(46) Inamdar, S. N.; Ingole, P. P.; Haram, S. K. Determination of Band Structure Parameters and the Quasi-Particle Gap of CdSe Quantum Dots by Cyclic Voltammetry. *ChemPhysChem* **2008**, *9* (17), 2574−2579.
(47) Jacobsson, T. J.; Edvinsson, T. Photoelectrochemical Determination of the Absolute Band Edge Positions as a Function of Particle Size for ZnO Quantum Dots. *J. Phys. Chem. C* **2012**, *116* (29), 15692−15701.
(48) Hwang, J.; Wan, A.; Kahn, A. Energetics of Metal-Organic Interfaces: New Experiments and Assessment of the Field. *Mater. Sci. Eng., R* **2009**, *64* (1−2), 1−31.
(49) Bürkle, M.; Lozac'h, M.; McDonald, C.; Mariotti, D.; Matsubara, K.; Švrček, V. Bandgap Engineering in OH-Functionalized Silicon Nanocrystals: Interplay between Surface Functionalization and Quantum Confinement. *Adv. Funct. Mater.* **2017**, *27*, 1701898−1701898.
(50) Kuriplach, J.; Šob, M.; Brauer, G.; Anwand, W.; Nicht, E.-M.; Coleman, P. G.; Wagner, N. Positron Affinity in Semiconductors: Theoretical and Experimental Studies. *Phys. Rev. B: Condens. Matter Mater. Phys.* **1999**, *59* (3), 1948−1955.
(51) Kaisheva, L. I. Surface Ionization of Alkali-Metal Atoms on Sic Single-Crystals. *Phys. Solid State* **1973**, *14*, 2108.
(52) Pelletier, J.; Gervais, D.; Pomot, C. Application of Wide-Gap Semiconductors to Surface Ionization: Work Functions of AlN and SiC Single Crystals. *J. Appl. Phys.* **1984**, *55* (4), 994.
(53) Zhang, Z.; Dai, Y.; Yu, L.; Guo, M.; Huang, B.; Whangbo, M.-H. The Surface Termination Effect on the Quantum Confinement and Electron Affinities of 3C-SiC Quantum Dots: A First-Principles Study. *Nanoscale* **2012**, *4* (5), 1592.
(54) Wu, X. L.; Fan, J. Y.; Qiu, T.; Yang, X.; Siu, G. G.; Chu, P. K. Experimental Evidence for the Quantum Confinement Effect in 3C-SiC Nanocrystallites. *Phys. Rev. Lett.* **2005**, *94* (2), 026102.
(55) Reboredo, F. A.; Pizzagalli, L.; Galli, G. Computational Engineering of the Stability and Optical Gaps of SiC Quantum Dots. *Nano Lett.* **2004**, *4* (5), 801−804.
(56) Brus, L. Electronic Wave Functions in Semiconductor Clusters: Experiment and Theory. *J. Phys. Chem.* **1986**, *90* (12), 2555−2560.
(57) Madelung, O. *Semiconductors: Data Handbook*, 3rd ed.; Springer: Berlin, 2004. DOI: 10.1007/978-3-642-18865-7.
(58) Perdew, J. P.; Burke, K.; Ernzerhof, M. Generalized Gradient Approximation Made Simple. *Phys. Rev. Lett.* **1996**, *77*, 3865; *Phys. Rev. Lett.* **1997**, *78* (7), 1396−1396.
(59) Weigend, F.; Ahlrichs, R. Balanced Basis Sets of Split Valence, Triple Zeta Valence and Quadruple Zeta Valence Quality for H to Rn: Design and Assessment of Accuracy. *Phys. Chem. Chem. Phys.* **2005**, *7* (18), 3297.
(60) Weigend, F. Accurate Coulomb-Fitting Basis Sets for H to Rn. *Phys. Chem. Chem. Phys.* **2006**, *8* (9), 1057.
(61) van Setten, M. J.; Weigend, F.; Evers, F. The GW -Method for Quantum Chemistry Applications: Theory and Implementation. *J. Chem. Theory Comput.* **2013**, *9* (1), 232−246.
(62) Kühn, M.; Weigend, F. One-Electron Energies from the Two-Component GW Method. *J. Chem. Theory Comput.* **2015**, *11* (3), 969−979.
(63) Hybertsen, M. S.; Louie, S. G. Electron Correlation in Semiconductors and Insulators: Band Gaps and Quasiparticle Energies. *Phys. Rev. B: Condens. Matter Mater. Phys.* **1986**, *34* (8), 5390−5413.
(64) *TURBOMOLE*, ver. 7.2; TURBOMOLE GmbH: Karlsruhe, Germany, 2017 (http://www.turbomole.com).

https://dx.doi.org/10.1021/acs.jpclett.9b03828
J. Phys. Chem. Lett. 2020, 11, 1721−1728